

A Microwave-Induced Thermoacoustic Imaging System With Non-Contact Ultrasound Detection

Ajay Singhvi¹, *Student Member, IEEE*, Kevin C. Boyle, *Student Member, IEEE*,
Mojtaba Fallahpour, *Member, IEEE*, Butrus T. Khuri-Yakub, *Fellow, IEEE*,
and Amin Arbabian, *Senior Member, IEEE*

Abstract—Portable and easy-to-use imaging systems are in high demand for medical, security screening, nondestructive testing, and sensing applications. We present a new microwave-induced thermoacoustic imaging system with non-contact, airborne ultrasound (US) detection. In this system, a 2.7 GHz microwave excitation causes differential heating at interfaces with dielectric contrast, and the resulting US signal via the thermoacoustic effect travels out of the sample to the detector in air at a standoff. The 65 dB interface loss due to the impedance mismatch at the air-sample boundary is overcome with high-sensitivity capacitive micromachined ultrasonic transducers with minimum detectable pressures (MDPs) as low as 278 $\mu\text{Pa}_{\text{rms}}$ and we explore two different designs—one operating at a center frequency of 71 kHz and another at a center frequency of 910 kHz. We further demonstrate that the air-sample interface presents a tradeoff with the advantage of improved resolution, as the change in wave velocity at the interface creates a strong focusing effect alongside the attenuation, resulting in axial resolutions more than 10 \times smaller than that predicted by the traditional speed/bandwidth limit. A piecewise synthetic aperture radar (SAR) algorithm modified for US imaging and enhanced with signal processing techniques is used for image reconstruction, resulting in mm-scale lateral and axial image resolution. Finally, measurements are conducted to verify simulations and demonstrate successful system performance.

Index Terms—Capacitive micromachined ultrasonic transducer (CMUT), non-contact microwave-induced thermoacoustics, piecewise synthetic aperture, ultrasound (US) imaging.

I. INTRODUCTION

PORTABLE imaging systems are in demand for a variety of applications, from nondestructive testing and sensing to security screening and point-of-care diagnostic imaging [1]–[3]. Such systems must also be low-cost, safe,

and easily field operable to realize their potential [4], [5] and have been made possible by continuing advances in solid-state electronics. However, most such portable ultrasound (US) approaches require intimate mechanical contact with the sample. A non-contact or standoff imaging system, in contrast, could have more applications in field settings where contact with the target is not practical, including imaging in soil [6], [7], extreme environments, unreachable areas [8], and emergency care where sterile conditions are required. The flexibility inherent in non-contact operation can also reduce dependence on skilled operators, such as sonographers in medical US settings, and possibly open the door to automated high-throughput sensing systems. Autonomous operation of commonplace, low-cost non-contact systems could enable machine learning [9]–[14] on large data sets and unlock many new opportunities by allowing for highly repeatable and precise measurements.

Non-contact imaging capabilities are already available in traditional imaging systems such as magnetic resonance imaging (MRI) and CT radiography, but their large cost and size have not been easily scaled to portable form factors [15]. Consequently, these gold-standard imaging systems are restricted to laboratories or hospitals. Existing portable approaches are limited by the need to balance various tradeoffs to achieve non-contact operation. Microwave imaging systems, for instance, have several of these tradeoffs, including that between penetration depth and resolution [16], [17]. The two-way transmission through the interface is also limiting, along with self-interference inherent in transmitting and receiving in the same modality.

In contrast, US systems are limited by the need for intimate contact with the target, because the acoustic impedance mismatch between imaging samples (such as water, tissue, soil, or industrial materials) and air is four orders of magnitude. This causes a large (65 dB) attenuation in the pressure signal as the US wave passes through the air-sample interface, the implications of which will be studied in further detail in Section II. In a pure US non-contact imaging system, this attenuation would be applied *twice*, once on the transmit side and again as the reflected signal returned to the transducer. To compensate for this round-trip loss, an airborne US transmitter must generate a very high level of focal pressure (e.g., the work in [18] generates a pressure of 2.5 kPa in air, higher than the OSHA limit in the USA [19]) to get sufficient signal strength. Recently, there have been attempts to address

Manuscript received December 2, 2018; accepted June 22, 2019. Date of publication June 27, 2019; date of current version September 25, 2019. This work was supported in part by the Defense Advanced Research Projects Agency MEDS Program, in part by the Texas Instruments University Relations Program, and in part by the Advanced Research Projects-Energy Agency through the ROOTS program under Grant DE-AR0000825. (Ajay Singhvi and Kevin C. Boyle contributed equally to this work.) (Corresponding author: Ajay Singhvi.)

A. Singhvi, K. C. Boyle, and A. Arbabian are with the Electrical Engineering Department, Stanford University, Stanford, CA 94305 USA (e-mail: asinghvi@stanford.edu).

M. Fallahpour was with the Electrical Engineering Department, Stanford University, Stanford, CA 94305 USA. He is now with ANSYS, Inc., San Jose, CA 95134 USA.

B. T. Khuri-Yakub is with the Edward L. Ginzton Laboratory, Electrical Engineering Department, Stanford University, Stanford, CA 94305 USA.

Digital Object Identifier 10.1109/TUFFC.2019.2925592

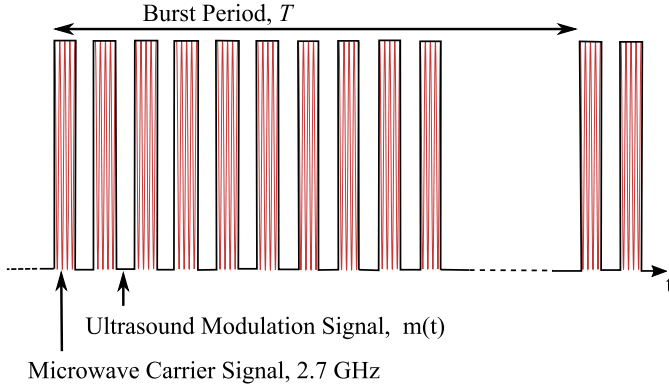


Fig. 2. Details of the modulation envelope applied to the microwave excitation. The modulation envelope corresponds to the frequency of the generated thermoacoustic pressure wave.

density Q (W/m^3) and it is derived from Poynting's theorem as in [39]

$$Q(\mathbf{r}, t) = \sigma(\mathbf{r})|\mathbf{E}(\mathbf{r}, t)|^2 + 2\pi f\epsilon_0\epsilon_r''(\mathbf{r})|\mathbf{E}(\mathbf{r}, t)|^2 + 2\pi f\mu_0\mu_r''(\mathbf{r})|\mathbf{H}(\mathbf{r}, t)|^2. \quad (1)$$

Based on (1), at each point \mathbf{r} , the amount of generated heat (the heating function, Q) depends on the frequency f , the conductivity σ , the vacuum electric permittivity ϵ_0 and magnetic permeability μ_0 , the imaginary parts of both the electric permittivity ϵ_r'' and the magnetic permeability μ_r'' of the absorbing media, and the root-mean-squared magnitudes of the electric and magnetic fields $|\mathbf{E}|$ and $|\mathbf{H}|$. For a wide range of materials, μ_r'' is typically zero; thus, the last term may be ignored [40]. This leaves the heating function dependent on only the dielectric properties, frequency, and the square of the magnitude of the electric field at each point.

The equation may suggest using higher frequencies to generate more heat; however, the skin depth effect limits the penetration depth for high-frequency signals. Therefore, there is a tradeoff in selecting the frequency of operation. For applications that require several centimeters of penetration inside soft materials, a microwave signal in the range of 1–3 GHz is required and our selection of 2.7 GHz for this system is therefore appropriate. On the other hand, the frequency of the produced thermoacoustic wave is dictated by the *envelope* of the EM wave [41], [42], and it should fall into the CMUT's operating frequency range. A new modulation scheme has been proposed to address this decoupled EM and TA frequency dependence in [22], [27], and [41]. In our adaptation of this scheme, the carrier signal is 2.7 GHz and the modulation signal $m(t)$ is a pulse train with a frequency equal to the center frequency of the CMUT and a 50% duty cycle. Fig. 2 depicts this microwave excitation signal, which is a modulated ON–OFF keying (OOK) pulse, where the burst period T determines the time between measurements. With this modulation scheme, $Q(\mathbf{r}, t)$ can be written as

$$Q(\mathbf{r}, t) = (Q_0(\mathbf{r}) + Q_{\text{HO}}(\mathbf{r}, t))|m(t)|^2 \quad (2)$$

where Q_0 and Q_{HO} show DC and higher order components of Q , respectively. As mentioned above, these higher order

components fall outside the CMUT's frequency range and can be ignored.

In this system, the microwave excitation at the carrier frequency has 2 kW peak power (average power limited to 7 W) and is applied using an open-ended waveguide (OEW) in contact with the sample. The OEW's high-peak power handling ability, low back-lobe radiation, and reasonable isolation make it a good candidate for this proof-of-concept microwave excitation unit. Depending on the sample, the OEW can be loaded with appropriate dielectric materials to improve its impedance matching. Note that, in the future work, the microwave excitation unit will also be engineered to work at a standoff, where beamforming can be used to deposit focused energy at depth [43].

2) *Thermoacoustic Waves*: The microwave excitation and absorption of EM energy by the sample results in an instantaneous temperature change ΔT [44]:

$$\Delta T = \int_{\Delta t} Q(\mathbf{r}, t)/(\rho C_p) dt \approx Q(\mathbf{r}, t)\Delta t/(\rho C_p) \quad (3)$$

where C_p is the heat capacity, and Δt is a short, “instantaneous” time over which the generated pressure does not travel significantly. This temperature change, which is typically in the milli-Kelvin range, can create a small fractional pressure p_0 [44]

$$p_0 = \beta \rho v_l^2 \Delta T. \quad (4)$$

By substituting (3) into (4), the instantaneous (normalized to Δt) induced thermoacoustic pressure at each point due to the microwave excitation can be calculated as in [44]:

$$p_0(\mathbf{r}, t) = \frac{\beta v_l^2 Q(\mathbf{r}, t)}{C_p} = \frac{\beta v_l^2}{C_p} |m(t)|^2 Q_0(\mathbf{r}) \quad (5)$$

where v_l is the speed of propagation of the longitudinal US wave in the medium and β is the thermal expansion coefficient. The difference between the dielectric properties of the target and that of the surrounding sample generates differential heating [$Q_0(\mathbf{r})$] and therefore differential pressure at this stage, which provides image contrast based on the dielectric properties of the target.

The induced TA pressure propagates through the medium, and its distribution $p(\mathbf{r}, t)$ as a function of position and time is calculated from the wave equation in [45]

$$\frac{\partial^2 p(\mathbf{r}, t)}{\partial t^2} - v_l^2 \nabla^2 p(\mathbf{r}, t) = \frac{\partial p_0(\mathbf{r}, t)}{\partial t}. \quad (6)$$

3) *Airborne Ultrasound Receiver Unit*: As alluded to in the previous sections, a major challenge of US-based non-contact imaging is the significant loss of signal as it is transmitted from the sample to air due to the large impedance mismatch. For example, air with $\rho = 1.225 \text{ kg}/\text{m}^3$, $v_l = 343 \text{ m}/\text{s}$, i.e., $Z = 420 \text{ Rayl}$ has a huge mechanical contrast with a tissue-mimicking agarose sample $\rho = 1000 \text{ kg}/\text{m}^3$, $v_l = 1450 \text{ m}/\text{s}$, i.e., $Z = 1.45 \times 10^6 \text{ Rayl}$ [46]. Thus, when the thermoacoustic signal leaves the sample to travel through air to the US receiver, the transmission coefficient is [47]

$$T = \frac{2Z_{\text{air}}}{Z_{\text{agarose}} + Z_{\text{air}}} = -64.7 \text{ dB}. \quad (7)$$

This large interface loss can be overcome with either a large excitation, which may be technically difficult or conflict with regulatory safety limits (whether of US [48], [49] or of microwave [19]), or with high-sensitivity US detectors together with coherent processing. Our system pursues the latter strategy of high sensitivity detectors realized with CMUTs.

The CMUTs used here are capacitive US sensors made of a thin vibrating plate over a vented cavity [50]. The low mechanical impedance of the thin plate provides an excellent impedance match with air, while the large DC electric field across the electrodes (plate and substrate) achieves a high electromechanical coupling coefficient approaching unity [51]. The vented cavity introduces squeeze film damping that increases bandwidth at the cost of some sensitivity, which is a fundamental tradeoff in the design of CMUTs [52]. Using the multi-parameter design approach described in [53], we design CMUTs tailored for NCTA imaging, with high sensitivity at the expense of a narrow bandwidth.

The aforementioned factors make CMUTs a favorable choice for use in the NCTA imaging system as other options such as piezoelectric transducers either require additional matching layers or are still under active investigation for optimized receive operation [54]–[56]. The relatively low receive sensitivity of commercially available microphones also precludes their use in a system that has to overcome challenging signal-to-noise constraints.

In this paper, we use two different CMUTs—one designed to operate at frequencies less than 100 kHz [23] and another operating at relatively higher frequencies closer to 1 MHz [53]. These operating frequencies were chosen to highlight their effect on various system parameters such as standoff distance, imaging resolution, and the different application spaces they might be best suited to. Systems with US propagation in air are limited to lower frequencies than typical contact US systems due to frequency-dependent attenuation. For instance, at 1 MHz, attenuation in air is 1.65 dB/cm, which would limit practical standoff distance to just a few centimeters (practical for emergency care situations [18], US-based wearables [57], [58], or nondestructive testing of materials in extreme conditions); whereas attenuation is significantly lower at lower US frequencies, e.g., 0.03 dB/cm at 100 kHz [59] and can afford much larger standoff distance (for remote-sensing applications such as an airborne SONAR system [8] or for below ground imaging [7]).

The CMUTs used here were characterized to find the bandwidth and frequency response with a laser Doppler vibrometer (LDV). The measurement result [Fig. 3(a)] shows that one of the CMUTs has a center frequency f_c of 71 kHz, with a 3.5% fractional bandwidth or a high quality factor q_f of 28.5. The other CMUT [Fig. 3(d)] has a higher center frequency f_c of 910 kHz, with an approximately 10% fractional bandwidth or a quality factor q_f of 9.1. Based on this characterization, a second-order pressure-to-voltage transfer function or filter is used to model the CMUT's normalized response

$$\tilde{G}(j\omega) = \frac{j\omega\omega_c/q_f}{\omega_c^2 - \omega^2 + j\omega\omega_c/q_f} \quad (8)$$

where $\omega_c = 2\pi f_c$.

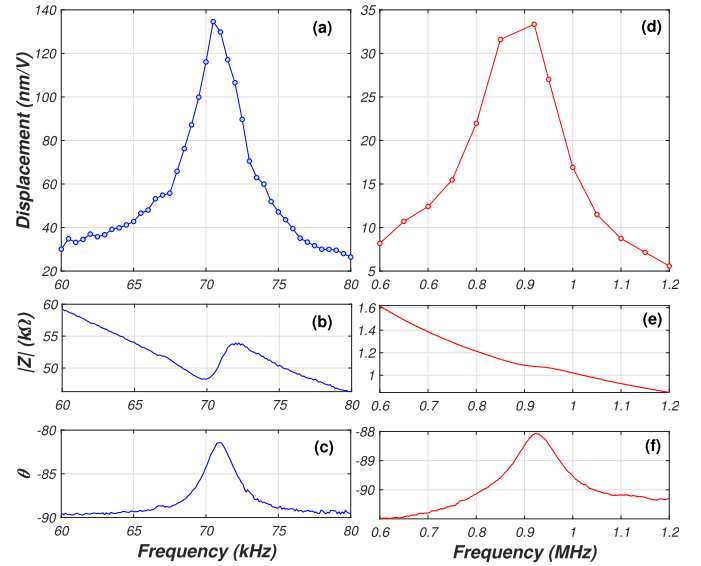


Fig. 3. Characterization measurements of the CMUTs. (a) and (d) LDV displacement measurement with respect to frequency. (b) and (e) Magnitude of impedance measurement with respect to frequency. (c) and (f) Phase of impedance measurement with respect to frequency, where the peak corresponds to the center frequency of the device under test.

Impedance measurements shown in Fig. 3(b) and (c), and (e) and (f) also show the resonant frequency and the magnitude of the phase peak corresponds to the resulting sensitivity, respectively. The sensitivity was measured with a pitch-catch measurement between two similar devices and a calibrated pressure microphone, described in our previous work [22], to determine the minimum detectable pressure (MDP) of the device used here. The MDP of the CMUT centered at 71 kHz was found to be as small as 278 $\mu\text{Pa}_{\text{rms}}$, while the one centered at 910 kHz had a higher MDP of 9 mPa_{rms} , as expected based on the sensitivity-bandwidth tradeoff discussed earlier [52] and due to the much wider bandwidth of the latter CMUT. The pitch-catch measurements also indicated that the beamwidth of the CMUTs was very wide, well over 90° . The CMUT characteristics and the challenges they impose on the stand-off imaging system are further discussed in later sections. Throughout the remainder of the paper, we will use the CMUT centered at 71 kHz as a guiding example, with final results shown for CMUTs operating at both 71 and 910 kHz.

The CMUTs are packaged on a pin grid array and mounted on a receiver PCB as shown in the inset of Fig. 4 interfaced with a single-stage resistive feedback transimpedance amplifier that provides a gain of 300 $\text{M}\Omega$ and is carefully matched to the impedance of the CMUT, including the added capacitance of the package, bond wires, and board trace. The copper mesh surrounding the CMUT and receiver provides shielding from EM interference that may leak into the receiver chain and it introduces only 1 dB of US attenuation. A digital oscilloscope synchronized with the microwave excitation pulse is used to capture the amplified CMUT signal. No averaging was applied to the oscilloscope, with other signal processing techniques used to improve received SNR which are discussed in detail in Sections V and VI.

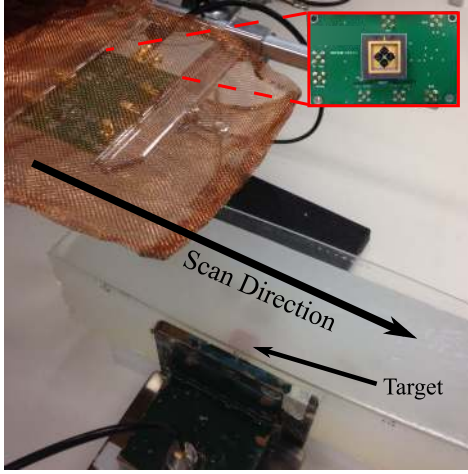


Fig. 4. Imaging system collecting data from the sample with one embedded target. Inset: close-up of the CMUT and receiver board is also provided.

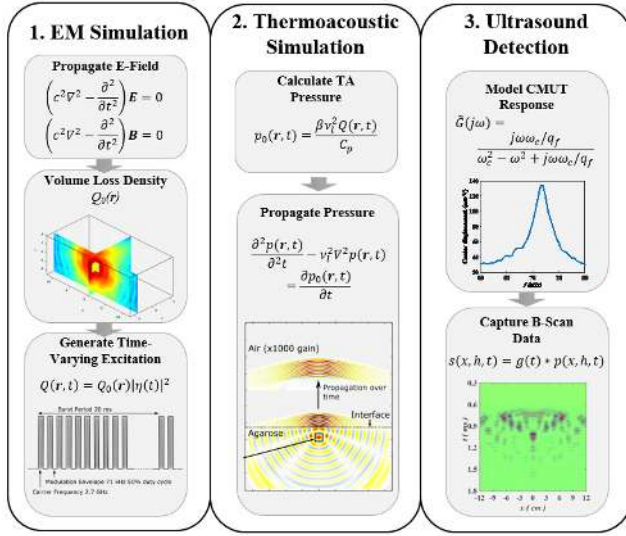


Fig. 5. Block diagram of the simulation framework.

III. SYSTEM MODELING AND SIMULATION

The full theoretical thermoacoustic framework is spread across both the EM and acoustic domains. Modeling the complex microwave, heating, stress, and acoustic interactions in realistic configurations requires a multiphysics simulation framework. This requirement motivated us to develop a simulation framework with the main blocks depicted in Fig. 5. We explain the details of the simulation setup through a specific example using the CMUT centered at 71 kHz as the US receiver. The example mimics a medical imaging scenario, where a sample is made of a rectangular block of agarose gel inside an acrylic mold with an embedded dielectric target. The sample is designed to approximate the electrical and US properties of human soft tissue ($\epsilon_r = 78.3 - j21.9$ at 2.7 GHz, $\rho = 1000 \text{ kg/m}^3$, speed of sound $v_l = 1450 \text{ m/s}$ [60]), which are verified through measurements with a dielectric probe and US pitch-catch experiments. The dielectric target is a cube 2 cm on each side with a low dielectric constant ($\epsilon_r = 5 - j0.1$,

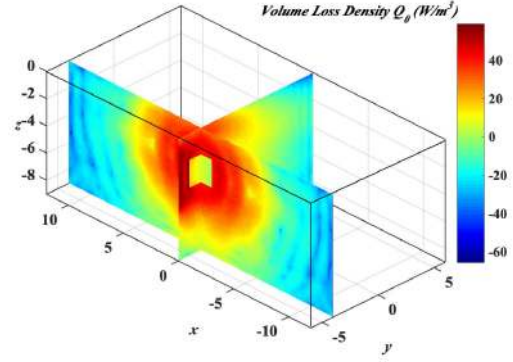


Fig. 6. Volume loss density Q_0 from HFSS simulation with 2-kW input (log scale). Note the small absorption within the dielectric target (length units: cm).

$\rho = 1500 \text{ kg/m}^3$, $v_l = 2000 \text{ m/s}$) to provide contrast with the agarose gel. The dielectric target is positioned 1 cm inside the agarose block from the waveguide excitation and 2 cm below the air boundary at the top of the agarose block. The CMUT is at standoff distance $L_1 = 20 \text{ cm}$ in air. The microwave source excites the embedded target from the side with the described modulation scheme to induce thermoacoustic signals at interfaces with dielectric contrast.

4) *Electromagnetic Domain Simulation*: To calculate the microwave-induced heat, the EM wave propagation from the waveguide source to the sample and target is simulated. Given the size and the heterogeneity of the solution domain, differential equation-based solvers such as ANSYS HFSS [61] are preferred over integral equation-based solvers. The entire scenario is simulated, and the volume loss profile is extracted as shown in Fig. 6. Note that the same coordinate system will be followed throughout, with the z -axis used to indicate the axial direction, and the x -axis used to indicate the lateral direction.

5) *Thermoacoustic Domain Simulation*: By applying (5), the volume loss profile $Q_0(\mathbf{r})$ is converted to TA pressure distribution. The TA pressure wave propagation inside the medium is then simulated by implementing the differential equation (6) in the time domain with a combination of pseudo-spectral and k -space techniques [62].

The pseudo-spectral method performs the spatial interpolation between grid points via a Fourier series implemented with the fast Fourier transform (FFT), requiring only half wavelength ($\lambda/2$) grid spacing, and the k -space method eases the restriction on the minimum time step required to maintain stability [62]. Both techniques contribute to significantly faster computation times compared to finite difference and finite element methods [63]. Based on this hybrid technique, the simulation was performed, and the result is shown in Fig. 7(a). This figure shows a snapshot view of the simulated US wave propagation for the sample under study (signals in air are amplified $1000\times$ to normalize the dynamic range of the signals in air and agarose given the large attenuation at the boundary). For comparison, the same simulation was performed with a homogeneous background (agarose), and the result is shown in Fig. 7(b). It is clear that for the

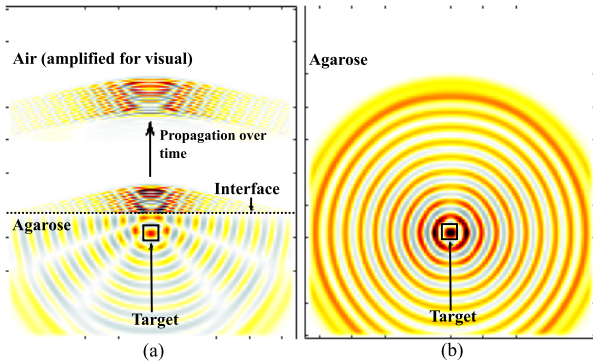


Fig. 7. Simulated wave propagation for an embedded target inside (a) layered air-agarose background with interference and diffraction effects from the acoustic impedance interface, and (b) homogeneous agarose background. Note that, in (a), the lines of destructive interference in the agarose layer and the focusing effect of the interface on the wavefront. Pressure values in the air layer have been increased 1000 \times to improve the dynamic range of the figure after the 65-dB interface loss.

heterogeneous background, the shape and curvature of the wavefronts in air versus the sample change significantly due to the refraction at the boundary. This refraction is proportional to the more than 4 \times difference in v_l governed by Snell's law [64]. Note the focusing effect of the boundary and the visible interference pattern generated by reflections from the boundary and the US interaction with the embedded target [Fig. 7(a)]. As this figure clearly shows, special considerations need to be made in the imaging algorithm to model the heterogeneous nature of the medium. Also, this focusing effect created at the air-agarose boundary has implications on the achievable resolution of the system, which are discussed in detail in Section IV.

6) *Ultrasound Detection Simulation*: Fig. 8(a) shows the calculated TA pressure signal at the CMUT location over time (A-scan) in response to a single pulse excitation. In the first case, only the air-agarose interface is modeled and the bottom and sides of the agarose layer are replaced with a perfectly matched layer (PML) that prevents reflections. The resulting pulse shape is a function of the spatial profile of $Q_0(\mathbf{r})$ and the excitation pulsewidth. In the second case, the bottom and sides of the agarose layer are modeled realistically. The same single pulse excitation agrees with the first case for the duration of the pulse, but the large reflections (multipath and multiple reflections) from all the boundaries in the simulation volume create signal clutter for milliseconds afterward. When multiple excitation pulses are used in a burst, such as the proposed 10-pulse excitation shown in Fig. 2, the resulting pressure signal is complicated by both the reflections and the superposition of the closely spaced pulses. The TA pressure for ten pulses is shown in Fig. 8(b) alongside the single pulse excitation with the realistic bottom and side boundaries. Although the initial peaks from the first pulse agree, the addition of multiple pulses makes the signal increasingly complex because the next pulse arrives before the spatial distribution of the first pulse has propagated all the way out of the agarose layer. The CMUT's limited bandwidth demands these multiple pulses (e.g., 10) be applied to the sample so the CMUT can ring

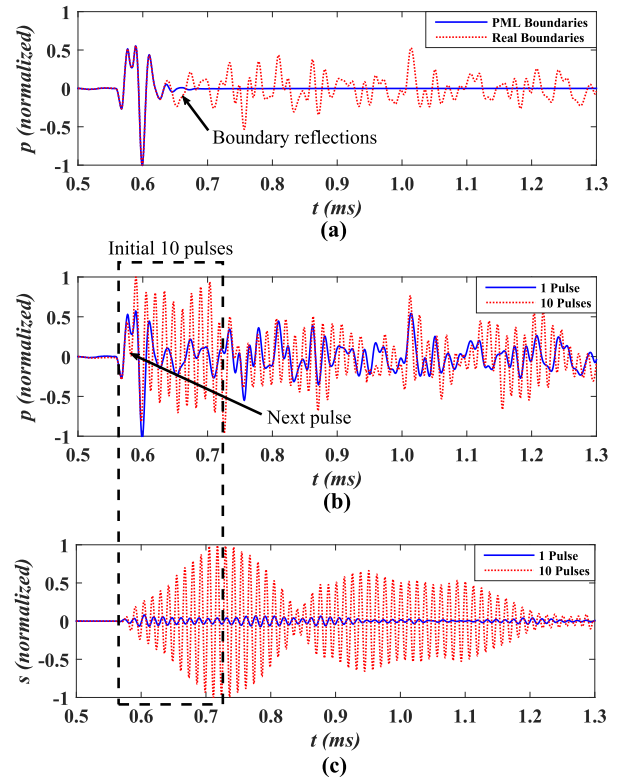


Fig. 8. Simulated A-scan data for several scenarios. (a) Single excitation pulse of a heterogeneous medium with PML boundaries on the sides and bottom of the agarose that prevent extraneous reflections compared with real boundaries to show expected behavior. (b) One and ten pulse excitations of a heterogeneous medium. (c) CMUT response to the one and ten pulse excitations of a heterogeneous medium.

up to full sensitivity and generate a large enough SNR for detection. Note that this effect is more pronounced for the high-sensitivity, high-quality-factor CMUT centered at 71 kHz than for the CMUT with the lower quality factor centered at 910 kHz.

The CMUT's response $s(x, y, z, t)$ to an incident signal can be calculated through the convolution of the TA pressure with the impulse response of the CMUT $g(t) \Leftrightarrow \tilde{G}(j\omega)$:

$$s(x, y, z, t) = g(t) * p(x, y, z, t). \quad (9)$$

Using this relationship, the CMUT responses to the TA pressure signals in Fig. 8(b) are shown in Fig. 8(c). The ten-pulse excitation better utilizes the sensitivity of the high-quality-factor CMUT, and the resulting voltage signal is more than 12 \times larger than that of the single pulse, resulting in SNR improvements that are critical for this system. This simulated signal is in agreement with our previous experimental observations in [22]–[24].

IV. RESOLUTION ANALYSIS

The narrow bandwidth of the highly sensitive CMUTs limits the achievable image resolution. The axial resolution (Δz) and lateral resolution (Δx) (using the coordinate system shown in Fig. 1) of an US imaging system depend on the depth of field (DOF) and the beamwidth (W_b) [65], respectively.

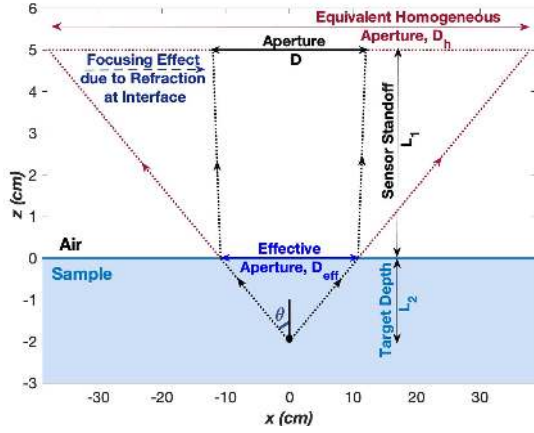


Fig. 9. Schematic of the focusing effect created as US waves travel from the sample to air.

This dependence is as follows:

$$\text{DOF} \propto \lambda (F_{\#})^2 \quad (10)$$

$$W_b \propto \lambda (F_{\#}) \quad (11)$$

where λ is the wavelength of US used and $F_{\#}$ refers to the focal number, which is

$$F_{\#} = \frac{\text{Target Depth}}{\text{Aperture Width}}. \quad (12)$$

A shallower DOF results in a shorter distance over which the US beam remains focused and hence better axial resolution, while a narrower beamwidth results in better lateral resolution. Thus, a higher US frequency (or smaller λ) and a smaller $F_{\#}$ lead to better system resolution. In this paper, we improve the system resolution by using synthetic aperture-based detection techniques [66]–[68] to increase the aperture width and hence decrease $F_{\#}$. However, note that (12) is applicable when imaging in a homogeneous background and needs to be modified to work for a heterogeneous background.

A schematic representation of the heterogeneous system geometry and the propagation of US waves from the sample to air is shown in Fig. 9. A single CMUT element is scanned to form a synthetic aperture of width D at a standoff height L_1 from the interface, with target located at depth L_2 . The change in wave velocity at the air–sample interface (Fig. 7) creates a focusing effect, resulting in the US waves refracting inward (black dotted lines) toward the CMUT receiver. To adapt (12) to the heterogeneous scenario of US waves being captured by the synthesized aperture D in air, we convert it to an entirely homogeneous situation—by back-projecting the US waves to be captured by an effective aperture D_{eff} at the air–sample interface instead. The exact value of D_{eff} can be calculated by solving a quartic equation that takes into account system geometry (L_1 , L_2 , D) as well as Snell’s law. On the other hand, if the entire distance between the target and the CMUT (i.e., $z = [-L_2, L_1]$) was homogeneous (as in contact-based imaging), the waves radiate continually outward (dotted red lines) and one would require a much larger equivalent aperture, D_h to capture the same amount of information as in the heterogeneous case. The resolution

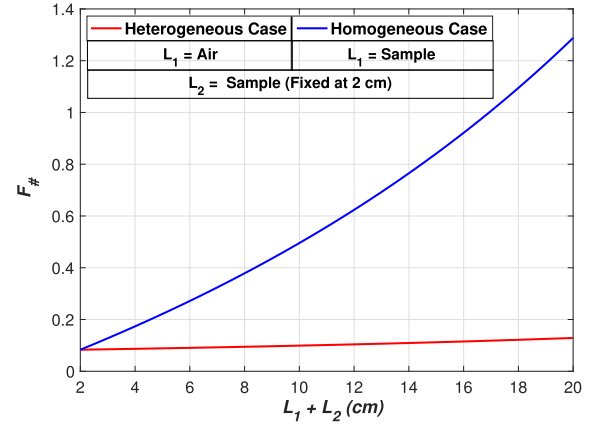


Fig. 10. Comparison of focal number between heterogeneous and homogeneous imaging scenarios.

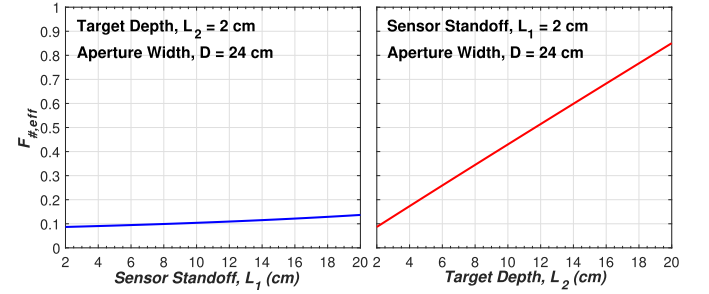


Fig. 11. Dependence of sensor standoff and target depth on the effective focal number for the NCTA imaging system.

limits in these two scenarios can be quantitatively compared by calculating the $F_{\#}$ for each case as seen in the following equations:

$$F_{\#, \text{homogeneous}} = \frac{L_1 + L_2}{D_h} \quad (13)$$

$$F_{\#, \text{heterogeneous}} = F_{\#, \text{eff}} = \frac{L_2}{D_{\text{eff}}}. \quad (14)$$

For the system geometry described in Fig. 9, with $D = 24$ cm and a fixed $L_2 = 2$ cm, one can see from Fig. 10 that the $F_{\#}$ is much smaller in the heterogeneous case, as opposed to the homogeneous scenario wherein the entire distance between the target and the CMUT (i.e., $z = [-L_2, L_1]$) was homogeneous. Thus, we can conclude that, for a fixed aperture width and a fixed distance ($L_1 + L_2$) between the target and CMUT, the resolution is much better in the case when the intervening medium is heterogeneous (air–sample) as opposed to entirely homogeneous (sample). Moreover, Fig. 11 shows that the effective focal number $F_{\#, \text{eff}}$ of the NCTA imaging system varies much more significantly with target depth in the sample as opposed to sensor standoff in air, enabling operation at large standoffs without significant loss in image resolution.

However, while $F_{\#}$ serves as a useful metric to appreciate such trends and comparisons, typical expressions [65] that relate the $F_{\#}$ to the image resolution use far-field approximations that may not always be valid. Instead, we estimate the resolution of the system by determining the k -space

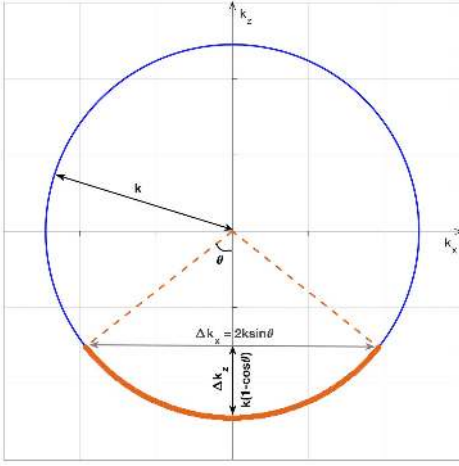


Fig. 12. Typical spatial frequency domain representation showing k -space support for a narrow bandwidth imaging system.

support [69] of the target, or in other words, by how much of the spatial frequency content of the target is captured by the sensor. This support is a function of the system geometry (represented by the $F_{\#,\text{eff}}$ or the viewing angle, θ) as well as the operating frequencies (and hence bandwidth) of the sensor. The sampled spatial frequency components of the target captured by the sensor can be calculated by considering that the wavevector lies in the spatial frequency plane on a circle, with radius equal to the wavenumber. Since the CMUTs used are narrowband, the k -space representation can be assumed to have a single circle with radius equal to the wavenumber corresponding to its operating frequency (a wideband sensor would have concentric circles of radii equal to wavenumbers bound by the highest and lowest operating frequency), with additional support provided by the system geometry. Fig. 12 shows the spatial frequency domain representation corresponding to Fig. 9, with the spatial resolution in a given direction given by the component of the wavevector in the corresponding k -axis. The axial (Δz) and lateral (Δx) resolutions can, thus, be given by the following equations:

$$\begin{aligned} \Delta z &= \frac{2\pi}{\Delta k_z} = \frac{2\pi}{k(1 - \cos \theta)} = \frac{\lambda}{1 - \cos \theta} \\ &= \frac{\lambda}{1 - \frac{1}{\sqrt{1 + D_{\text{eff}}^2/L_2^2}}} = \frac{\lambda}{1 - \frac{1}{\sqrt{1 + F_{\#,\text{eff}}^2}}} \end{aligned} \quad (15)$$

$$\begin{aligned} \Delta x &= \frac{2\pi}{\Delta k_x} = \frac{2\pi}{2k \sin \theta} = \frac{\lambda}{2 \sin \theta} \\ &= \frac{\lambda}{2\sqrt{1 + \frac{L_2^2}{D_{\text{eff}}^2}}} = \frac{\lambda}{2\sqrt{1 + F_{\#,\text{eff}}^2}}. \end{aligned} \quad (16)$$

As seen from (15) and (16), despite the narrowband nature of the CMUTs, one can achieve image resolution on the order of the wavelength, provided the imaging system has a small $F_{\#}$, which is achievable in this multi-layered imaging scenario due to the focusing effect as a result of refraction at the interface. For example, for the imaging scenario illustrated in Fig. 9, with the CMUT operating at 71 kHz (with a 2.5-kHz bandwidth), we can achieve an axial resolution of 3 cm,

which is more than $20\times$ smaller than that predicted by the traditional speed/bandwidth limit. The resolution limits and its dependence on system parameters (sensor standoff, aperture width, and target depth) for the NCTA system presented in this paper (set by the CMUT centered at 910 kHz) can be seen in Fig. 13.

V. IMAGE RECONSTRUCTION

As discussed in Section IV, we use synthetic aperture-based detection techniques to improve image resolution. However, conventional SAR algorithms are not suitable for this application without some modification. The SAR algorithm works by establishing a linear relationship between the collected samples of the wave (at spatially distributed positions) and the reflectivity of the target (or radiation of the source in our case). The adaptation of the SAR concept for US imaging has been reported under different names, such as synthetic aperture US imaging, synthetic aperture focusing technique (SAFT), and synthetic aperture acoustic imaging [70]–[72]. These imaging techniques all share similar underlying mathematical and physical foundations that can be explained using the f – k range migration algorithm [73]. They are fast, robust, and provide fine resolution and improved SNR. However, they were all initially developed for anomalies embedded in a homogeneous medium and cannot be used, without modification, for the non-contact case in which the propagation medium is heterogeneous, comprising both air and sample with very different propagation properties.

To accommodate heterogeneous media, the piecewise SAR algorithm proposed in [74] for microwave imaging is adapted to US imaging and used here. This algorithm takes into account the heterogeneity of the background media when it back-propagates the US wave. The PW-SAR algorithm converts the data collected by the scanning CMUT into the spectral domain. Mathematically, this conversion is based on the Weyl identity, and physically, it corresponds to decomposing spherical pressure waves into plane waves [75]. It then back-propagates those plane waves that are parallel to the air–sample interface in a piecewise manner (i.e., one layer at a time) to focus on the desired depth. This accounts for layers with different acoustic properties. Later, it transforms the back-propagated waves into the spatial domain and forms an image.

To implement the PW-SAR algorithm, the data collected at the scanning positions $s(x, z = L_1, t)$ is processed (e.g., time-filtered) and converted into frequency–spectral domain data $\tilde{S}(K_x, z = L_1, f)$. Then, it can be migrated back to create an image at (x', z') inside the sample, using the PW-SAR imaging equation

$$\Gamma(x', z') = \sum_f F_x^{-1} \{ \tilde{S}(k_x, z = L_1, f) \cdot \exp(j(k_{z,1}L_1 - k_{z,2}z')) \} \quad (17)$$

where $\Gamma(x', z')$ represents the image, F_x^{-1} represents the inverse Fourier transform, L_1 is the standoff distance (Fig. 1),

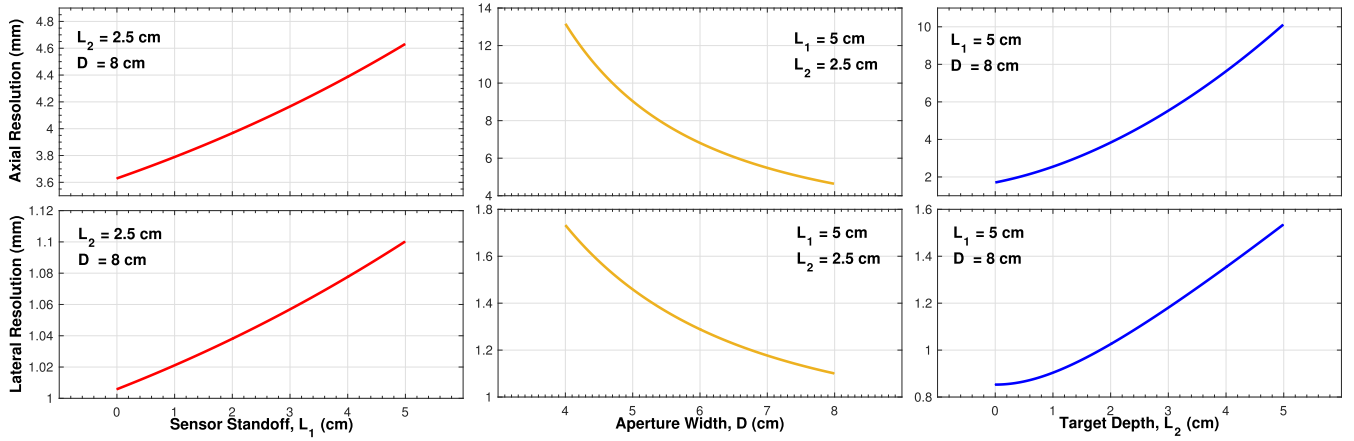


Fig. 13. Axial and lateral resolution limits of the NCTA system when using the CMUT centered at 910 kHz and its dependence of different system parameters.

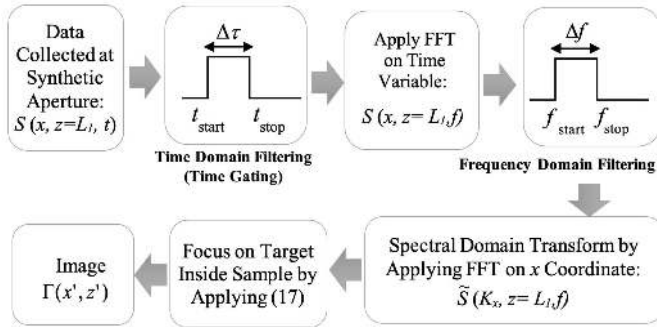


Fig. 14. Block diagram of signal processing and image reconstruction.

and $\tilde{\cdot}$ denotes the spectral domain representation. In contrast with [74], which was for a monostatic round-trip scenario, here, the target itself is an US source generated through the thermoacoustic effect. The dispersion relationship that governs the wave propagation should then be modified to

$$k_i^2 = k_{z,i}^2 + k_x^2. \quad (18)$$

Here, k_x , $k_{z,i}$ are components of the k_i vector in the x - and z -directions, respectively. In addition, $k_i = \omega/v_{l,i}$ is the wavenumber in the i th medium, where $i = 1$ is air and $i = 2$ is the sample.

Because the algorithm incorporates coherent processing and averaging, it also helps to improve SNR. The entire image reconstruction algorithm, which includes time and frequency filtering and signal processing, is summarized in Fig. 14. A comprehensive explanation of the PW-SAR algorithm and its implementation can be found in [74].

VI. SIMULATION AND MEASUREMENT RESULTS AND DISCUSSION

In this simulation scenario, we replicate the case under study in Sections III and IV, wherein a single CMUT element centered at 71 kHz is scanned over a line and a synthetic aperture is of 24 cm is created, extending from $x = -12$ cm to $x = 12$ cm. A cross-sectional view of the same is shown in Fig. 15(a). The simulation data collected for this scenario

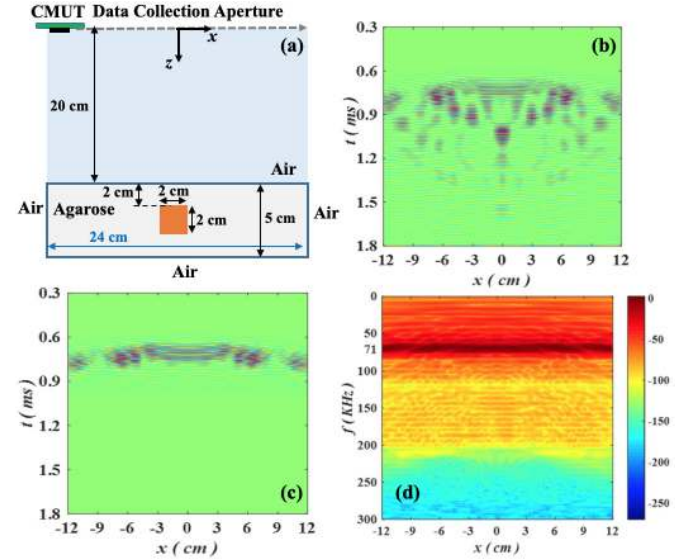


Fig. 15. (a) Cross-sectional view of imaging setup for CMUT centered at 71 kHz (b) collected raw data over all scanned positions, (c) processed data after time-gating signal, (d) amplitude (in decibels) of the time-gated signal transferred into the Fourier domain.

was processed to form an image, following the steps in Fig. 14. The data shown in Fig. 15(b), where each column is the thermoacoustic signal collected over time at the corresponding scan step, were filtered in the time domain to reduce the unwanted multipath, multiple reflections, and RF interference, which resulted in the cleaner data shown in Fig. 15(c). The maximum desired range, the CMUT's standoff distance, and the CMUT's quality factor dictate the start (t_{start}) and stop (t_{stop}) times. Gaussian time gating is used to avoid sharp start and stop and minimize the generation of high-frequency artifacts.

Since PW-SAR works with frequency-spectral domain data, the time-gated signal was converted into the frequency domain by performing an FFT on the time variable. The converted data are shown in Fig. 15(d). The Fourier domain signal was filtered to reduce out-of-band interference and noise. The start (f_{start}) and stop (f_{stop}) frequencies were selected

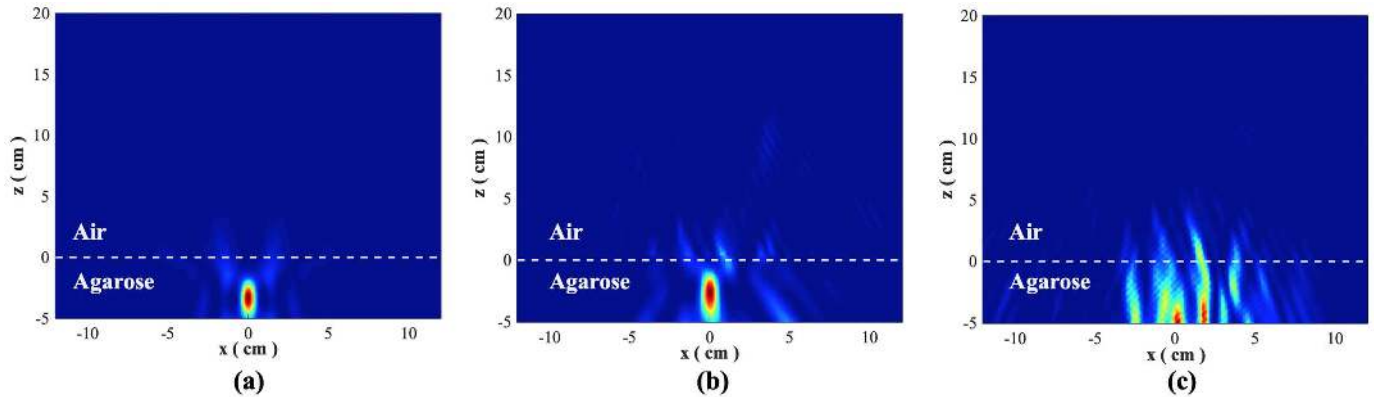


Fig. 16. Reconstructed image for single target case using (a) PW-SAR from simulation data, (b) PW-SAR from measurement data, and (c) conventional SAR from measurement data.

to be 69.75 and 72.25 kHz based on the CMUT's frequency response from Fig. 3. Fig. 15(d) also proves that most of the signal power is limited to this bandwidth. This preprocessed data was then input to the PW-SAR algorithm to produce an image, as shown in Fig. 16(a). The gamma correction was applied to the image to increase the contrast between target indications and background clutter, and the maximum depth was set to 5 cm to avoid artifacts that fall outside the region of interest. There is a clear indication of the target at the correct location. The PW-SAR algorithm together with the time-gating contributes to getting the predicted resolution in this example.

A measurement setup mimicking the case studied above was developed to verify the performance of the simulation tool and the proposed system. The data were collected from the CMUT board via a digital oscilloscope and processed in the same way explained in Fig. 14. The resulting image is shown in Fig. 16(b); this image is in good agreement with the simulation results. For comparison, the processed data were also used to construct an image using a conventional SAR algorithm. The resulting image, shown in Fig. 16(c), does not provide any information about the target. This was expected since the conventional SAR algorithm does not take into account the widely differing speed of sound in air and in agarose. In this case, the speed of sound of the whole medium was considered to be equal to that of air. As a result, the target indication is at the incorrect depth and smeared out in range well past the bottom of the image domain, and multiple artifacts are created.

The configuration used for measurement with the CMUT centered at 910 kHz is similar to the first, except that the target size chosen was smaller to demonstrate the improved resolution that is possible. The measurement configuration, along with the reconstructed image, is shown in Fig. 17(a). As before, the CMUT was scanned to form a synthetic aperture, but at a relatively smaller aperture width of 8 cm with a step size of $\Delta x = 0.15$ mm. The reconstructed image is shown in Fig. 17(b). Fig. 18(a) shows the lateral point spread function that has a full-width half-maximum of 1.1 mm, and Fig. 18(b) shows the axial point spread function that has a full-width half-maximum of 4.7 mm, which completely determine the lateral and axial resolutions [76] of the system.

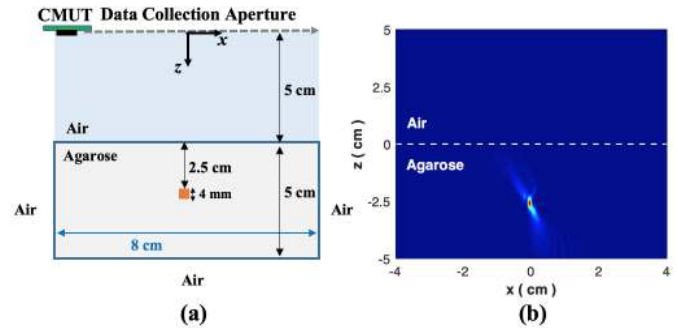


Fig. 17. (a) Cross sectional view of imaging setup for CMUT centered at 910 kHz. (b) Image reconstructed from measurement data.

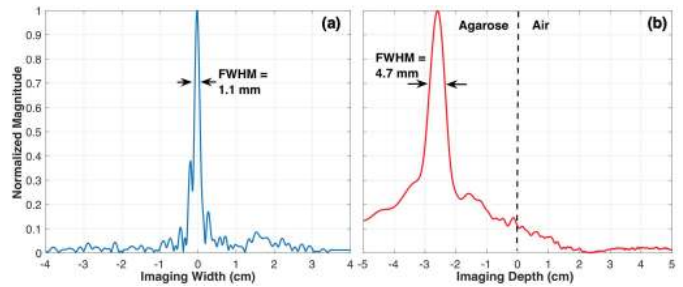


Fig. 18. Measured (a) lateral point spread function and (b) axial point spread function demonstrating resolution provided by CMUT centered at 910 kHz.

They are in good agreement with the numbers predicted in Section IV (Fig. 13) by determining the k -space support for this heterogeneous imaging scenario.

The images presented here demonstrate the feasibility and basic performance of our NCTA imaging system, but there are a large number of system design choices that may be tuned to different applications. While we scan a single CMUT to form a wide aperture, one could also integrate an array of CMUTs to form a real aperture and achieve real-time image formation. An array could also be applied to form 2-D real or synthetic apertures, which would be an improvement over the 1-D apertures used here and enable volumetric (3-D) imaging.

At the broader system level, improved axial resolution may also be possible with multi-frequency CMUT arrays and

stepped-frequency continuous-wave (SFCW) processing techniques, which are the focus of ongoing work [23], [77]–[79]. Increased resolution can also be achieved with optimized wideband CMUTs, or improved applicators for the microwave excitation that optimize the beam pattern distribution and heating profile [43], [80]. Finally, application of more advanced signal processing techniques (e.g., adaptive filtering [81], [82]), as well as more sophisticated imaging algorithms (e.g., forward iterative solvers [83]–[88]), would help further improve the images.

VII. CONCLUSION

A non-contact microwave-induced thermoacoustic imaging system that can, from the air, remotely image targets embedded inside opaque solid samples was presented. Signal generation is based on the thermoacoustic effect, where US signals are generated by a microwave excitation at dielectric contrast interfaces and detected at a standoff in air, despite significant loss in signal due to the acoustic impedance mismatch at the air–sample boundary. This was made possible by the use of high-sensitivity CMUTs with low MDPs. Both multiphysics simulations and theory illustrate the thermoacoustic generation mechanism and they, along with a piecewise SAR reconstruction algorithm developed for non-contact US imaging, were used to predict and evaluate system performance. A robust system-resolution analysis was also presented that is applicable to any non-contact US-based hybrid imaging modality. It was shown that system resolution did not vary much with sensor standoff in air and was substantially improved due to refraction occurring at the air–target interface. The realized system was then used to produce accurate images of target configurations using different US operating frequencies, demonstrating mm-scale resolution capabilities. Future work will focus on improved real-time, higher resolution imaging through multi-frequency CMUT arrays and SFCW measurement techniques and their development for specific applications. Further improvements are possible with advanced signal processing techniques, electronically steered microwave excitation, and beamformed US receiver arrays.

ACKNOWLEDGMENT

The views and opinions of authors expressed herein do not necessarily state or reflect those of the United States Government or any agency thereof.

REFERENCES

- [1] L. L. P. Wong, A. I. Chen, A. S. Logan, and J. T. W. Yeow, “An FPGA-based ultrasound imaging system using capacitive micromachined ultrasonic transducers,” *IEEE Trans. Ultrason., Ferroelectr., Freq. Control*, vol. 59, no. 7, pp. 1513–1520, Jul. 2012.
- [2] M. T. Ghasr, M. A. Abou-Khousa, S. Kharkovsky, R. Zoughi, and D. Pommerenke, “Portable real-time microwave camera at 24 GHz,” *IEEE Trans. Antennas Propag.*, vol. 60, no. 2, pp. 1114–1125, Feb. 2012.
- [3] A. T. Mobashsher, A. M. Abbosh, and Y. Wang, “Microwave system to detect traumatic brain injuries using compact unidirectional antenna and wideband transceiver with verification on realistic head phantom,” *IEEE Trans. Microw. Theory Techn.*, vol. 62, no. 9, pp. 1826–1836, Sep. 2014.
- [4] K. Chen, H.-S. Lee, and C. G. Sodini, “A column-row-parallel ASIC architecture for 3-D portable medical ultrasonic imaging,” *IEEE J. Solid-State Circuits*, vol. 51, no. 3, pp. 738–751, Mar. 2016.
- [5] H. Nan and A. Arbabian, “Peak-power-limited frequency-domain microwave-induced thermoacoustic imaging for handheld diagnostic and screening tools,” *IEEE Trans. Microw. Theory Techn.*, vol. 65, no. 7, pp. 2607–2616, Jul. 2017.
- [6] J. Coe and S. J. Brandenburg, “Cone penetration test—Based ultrasonic probe for p-wave reflection imaging of embedded objects,” *J. Bridge Eng.*, vol. 17, no. 6, pp. 940–950, Oct. 2011.
- [7] A. Delgado *et al.*, “Ground penetrating radar: A case study for estimating root bulking rate in cassava (*Manihot esculenta* Crantz),” *Plant Methods*, vol. 13, no. 1, p. 65, Dec. 2017.
- [8] D. Farrant, J. Burke, L. Dickinson, P. Fairman, and J. Wendoloski, “Opto-acoustic underwater remote sensing (OAURS)—An optical sonar?” in *Proc. IEEE SYDNEY*, May 2010, pp. 1–7.
- [9] T. Tan, B. Platel, R. Mus, L. Tabar, R. M. Mann, and N. Karssemeijer, “Computer-aided detection of cancer in automated 3-D breast ultrasound,” *IEEE Trans. Med. Imag.*, vol. 32, no. 9, pp. 1698–1706, Sep. 2013.
- [10] S. K. Davis, B. D. V. Veen, S. C. Hagness, and F. Kelcz, “Breast tumor characterization based on ultrawideband microwave backscatter,” *IEEE Trans. Biomed. Eng.*, vol. 55, no. 1, pp. 237–246, Jan. 2008.
- [11] L. Wei, Y. Yang, R. M. Nishikawa, and Y. Jiang, “A study on several Machine-learning methods for classification of Malignant and benign clustered microcalcifications,” *IEEE Trans. Med. Imag.*, vol. 24, no. 3, pp. 371–380, Mar. 2005.
- [12] H. Nan, B. A. Haghi, and A. Arbabian, “Interferogram-based breast tumor classification using microwave-induced thermoacoustic imaging,” in *Proc. IEEE Eng. Med. Biol. Soc. (EMBC)*, Aug. 2015, pp. 2717–2720.
- [13] H. Nan, T.-C. Chou, and A. Arbabian, “Segmentation and artifact removal in microwave-induced thermoacoustic imaging,” in *Proc. 36th Annu. Int. Conf. IEEE Eng. Med. Biol. Soc.*, Aug. 2014, pp. 4747–4750.
- [14] H. Nan, B. A. Haghi, M. S. Aliroth, M. Fallahpour, and A. Arbabian, “Fast iterative reconstruction algorithm for microwave-induced thermoacoustic imaging,” in *Proc. IEEE Biomed. Circuits Syst. Conf. (BioCAS)*, Oct. 2016, pp. 1–4.
- [15] M. Sarraçanie, C. D. LaPierre, N. Salameh, D. E. J. Waddington, T. Witzel, and M. S. Rosen, “Low-cost high-performance MRI,” *Sci. Rep.*, vol. 5, Oct. 2015, Art. no. 15177.
- [16] J. D. Shea, P. Kosmas, B. D. V. Veen, and S. C. Hagness, “Contrast-enhanced microwave imaging of breast tumors: A computational study using 3D realistic numerical phantoms,” *Inverse Problems*, vol. 26, no. 7, 2010, Art. no. 074009.
- [17] X. Li and S. C. Hagness, “A confocal microwave imaging algorithm for breast cancer detection,” *IEEE Microw. Wireless Compon. Lett.*, vol. 11, no. 3, pp. 130–132, Mar. 2001.
- [18] G. T. Clement, H. Nomura, H. Adachi, and T. Kamakura, “The feasibility of non-contact ultrasound for medical imaging,” *Phys. Med. Biol.*, vol. 58, no. 18, p. 6263, Aug. 2013.
- [19] I.-S. S. Board, “IEEE standard for safety levels with respect to human exposure to radio frequency electromagnetic fields, 3 kHz to 300 GHz,” IEEE, New York, NY, USA, Tech. Rep. IEEE Std C95.1-2005, Apr. 2006.
- [20] G. Rousseau, A. Blouin, and J.-P. Monchalain, “Non-contact photoacoustic tomography and ultrasonography for tissue imaging,” *Biomed. Opt. Express*, vol. 3, no. 1, pp. 16–25, 2012.
- [21] Y. Qin, P. Ingram, X. Wang, T. Qin, H. Xin, and R. S. Witte, “Non-contact thermoacoustic imaging based on laser and microwave vibrometry,” in *Proc. IEEE Int. Ultrason. Symp.*, Sep. 2014, pp. 1033–1036.
- [22] H. Nan *et al.*, “Non-contact thermoacoustic detection of embedded targets using airborne-capacitive micromachined ultrasonic transducers,” *Appl. Phys. Lett.*, vol. 106, no. 8, Feb. 2015, Art. no. 084101.
- [23] K. C. Boyle *et al.*, “Non-contact thermoacoustic imaging of tissue with airborne ultrasound detection,” in *Proc. IEEE Int. Ultrason. Symp. (IUS)*, Oct. 2015, pp. 1–4.
- [24] K. C. Boyle, H. Nan, B. T. Khuri-Yakub, and A. Arbabian, “Noncontact thermoacoustic detection of targets embedded in dispersive media,” *Proc. SPIE*, vol. 21, pp. 1–7, Oct. 2016.
- [25] D. R. Bauer, X. Wang, J. Vollin, H. Xin, and R. S. Witte, “Thermoacoustic imaging and spectroscopy for enhanced breast cancer detection,” in *Proc. IEEE Int. Ultrason. Symp.*, Oct. 2011, pp. 2364–2367.
- [26] R. A. Kruger, W. L. Kiser, K. D. Miller, and H. E. Reynolds, “Thermoacoustic CT,” in *IEEE MTT-S Int. Microw. Symp. Dig.*, May 2000, pp. 933–936.
- [27] L. V. Wang, “Microwave-induced acoustic (thermoacoustic) tomography,” in *Proc. Photoacoustic Imag. Spectrosc.*, Dec. 2017, pp. 339–348.
- [28] M. Xu and L. V. Wang, “Photoacoustic imaging in biomedicine,” *Rev. Sci. Instrum.*, vol. 77, no. 4, 2006, Art. no. 041101.

- [29] R. A. Kruger, "Thermoacoustic computed tomography of the breast," in *Proc. Photoacoustic Imag. Spectrosc.*, Mar. 2009, pp. 331–338.
- [30] G. Ku and L. V. Wang, "Scanning microwave-induced thermoacoustic tomography: Signal, resolution, and contrast," *Med. Phys.*, vol. 28, no. 1, pp. 4–10, Jan. 2001.
- [31] G. Ku, X. Wang, G. Stoica, and L. V. Wang, "Multiple-bandwidth photoacoustic tomography," *Phys. Med. Biol.*, vol. 49, no. 7, p. 1329, Mar. 2004.
- [32] K. Maslov, H. F. Zhang, S. Hu, and L. V. Wang, "Optical-resolution photoacoustic microscopy for in vivo imaging of single capillaries," *Opt. Lett.*, vol. 33, no. 9, pp. 929–931, 2008.
- [33] K. K. Shung, *Diagnostic Ultrasound: Imaging Blood Flow Measurements*. CRC Press, 2006.
- [34] R. Haupt, C. Wynn, B. Anthony, J. Fincke, A. Samir, and X. Zhang, "Non-contact laser ultrasound concept for biomedical imaging," in *Proc. IEEE Int. Ultrason. Symp. (IUS)*, Sep. 2017, pp. 1–5.
- [35] Z. Ji, Y. Fu, and S. Yang, "Microwave-induced thermoacoustic imaging for early breast cancer detection," *J. Innov. Opt. Health Sci.*, vol. 6, no. 1, Jan. 2013, Art. no. 1350001.
- [36] S. S. Chaudhary, R. K. Mishra, A. Swarup, and J. M. Thomas, "Dielectric properties of normal & malignant human breast tissues at radiowave & microwave frequencies," *Indian J. Biochem. Biophys.*, vol. 21, no. 1, pp. 76–79, 1984.
- [37] A. J. Surowiec, S. S. Stuchly, J. R. Barr, and A. Swarup, "Dielectric properties of breast carcinoma and the surrounding tissues," *IEEE Trans. Biomed. Eng.*, vol. 35, no. 4, pp. 257–263, Apr. 1988.
- [38] J. A. Zagzebski, *Essentials Ultrasound Physics*. St. Louis, MO, USA: Mosby, 1996.
- [39] D. Pozar, *Microwave Engineering*, 4th ed. Hoboken, NJ, USA: Wiley, 2005.
- [40] M. Omar, S. Kellnberger, G. Sergiadis, D. Razansky, and V. Ntziachristos, "Near-field thermoacoustic imaging with transmission line pulsers," *Med. Phys.*, vol. 39, no. 7, pp. 4460–4466, Jul. 2012.
- [41] H. Nan and A. Arbabian, "Stepped-frequency continuous-wave microwave-induced thermoacoustic imaging," *Appl. Phys. Lett.*, vol. 104, Jun. 2014, Art. no. 224104.
- [42] G. J. Diebold, T. Sun, and M. I. Khan, "Photoacoustic monopole radiation in one, two, and three dimensions," *Phys. Rev. Lett.*, vol. 67, no. 24, pp. 3384–3387, Dec. 1991.
- [43] H. Nan, S. Liu, G. J. Buckmaster, and A. Arbabian, "Beamforming microwave-induced thermoacoustic imaging for screening applications," *IEEE Trans. Microw. Theory Techn.*, vol. 67, no. 1, pp. 464–474, Jan. 2019.
- [44] C. G. A. Hoelen and F. F. M. de Mul, "A new theoretical approach to photoacoustic signal generation," *J. Acoust. Soc. Amer.*, vol. 106, pp. 695–706, May 1999.
- [45] Y. Xu and L. V. Wang, "Effects of acoustic heterogeneity in breast thermoacoustic tomography," *IEEE Trans. Ultrason., Ferroelectr., Freq. Control*, vol. 50, no. 9, pp. 1134–1146, Sep. 2003.
- [46] P. Filippi, D. Habault, J. P. Lefebvre, and A. Bergassoli, *Acoustics: Basic Physics, Theory, and Methods*. Amsterdam, The Netherlands: Elsevier, 1999.
- [47] G. S. Kino, *Acoustic Waves: Devices, Imaging, and Analog Signal Processing*. Upper Saddle River, NJ, USA: Prentice-Hall, 1987.
- [48] FDA, "Information for manufacturers seeking marketing clearance of diagnostic ultrasound systems and transducers," FDA, Tech. Rep. guidance number 560, 2008.
- [49] ACGIH, "TLVs and BEIs based on the documentation of the threshold limit values for chemical substances and physical agents & biological exposure indices," ACGIH, Tech. Rep., 2012.
- [50] N. Apte, K. K. Park, and B. T. Khuri-Yakub, "Experimental evaluation of CMUTs with vented cavities under varying pressure," in *Proc. IEEE Int. Ultrason. Symp. (IUS)*, Jul. 2013, pp. 1724–1727.
- [51] G. G. Yeralioglu, A. S. Ergun, B. Bayram, E. Haeggstrom, and B. T. Khuri-Yakub, "Calculation and measurement of electromechanical coupling coefficient of capacitive micromachined ultrasonic transducers," *IEEE Trans. Ultrason., Ferroelectr., Freq. Control*, vol. 50, no. 4, pp. 449–456, Apr. 2003.
- [52] N. Apte, K. K. Park, A. Nikoozadeh, and B. T. Khuri-Yakub, "Bandwidth and sensitivity optimization in CMUTs for airborne applications," in *Proc. IEEE Int. Ultrason. Symp.*, Sep. 2014, pp. 166–169.
- [53] B. Ma, C. Chang, H. K. Oğuz, K. Firouzi, B. T. Khuri-Yakub, and E. L. G. Lab, "Multi-parameter optimization of vented CMUTs for airborne applications," in *Proc. IEEE Int. Ultrason. Symp. (IUS)*, Sep. 2017, pp. 1–4.
- [54] T. E. G. Alvarez-Arenas, "Acoustic impedance matching of piezoelectric transducers to the air," *IEEE Trans. Ultrason., Ferroelectr., Freq. Control*, vol. 51, no. 5, pp. 624–633, May 2004.
- [55] M. D. Williams, B. A. Griffin, T. N. Reagan, J. R. Underbrink, and M. Sheplak, "An AlN MEMS piezoelectric microphone for aeroacoustic applications," *J. Microelectromech. Syst.*, vol. 21, no. 2, pp. 270–283, 2012.
- [56] Y. Kusano *et al.*, "Effects of DC bias tuning on air-coupled PZT piezoelectric micromachined ultrasonic transducers," *J. Microelectromech. Syst.*, vol. 27, no. 2, pp. 296–304, Apr. 2018.
- [57] I. AlMohimeed, H. Turkistani, and Y. Ono, "Development of wearable and flexible ultrasonic sensor for skeletal muscle monitoring," in *Proc. IEEE Int. Ultrason. Symp. (IUS)*, Jul. 2013, pp. 1137–1140.
- [58] A. Huang, M. Yoshida, Y. Ono, and S. Rajan, "Continuous measurement of arterial diameter using wearable and flexible ultrasonic sensor," in *Proc. IEEE Int. Ultrason. Symp. (IUS)*, Sep. 2017, pp. 1–4.
- [59] L. Jakevicius and A. Demcenko, "Ultrasound attenuation dependence on air temperature in closed chambers," *Ultragarsas*, vol. 63, no. 1, pp. 18–22, 2003.
- [60] P. Hasegall *et al.*, (2015). *ITIS Database for Thermal and Electromagnetic Parameters of Biological Tissues*. [Online]. Available: www.itis.ethz.ch/database
- [61] *Version 15.0.0*, HFSS, Ansys, Canonsburg, PA, USA, 2017.
- [62] B. E. Treeby and B. T. Cox, "k-Wave: MATLAB toolbox for the simulation and reconstruction of photoacoustic wave fields," *J. Biomed. Opt.*, vol. 15, no. 2, 2010, Art. no. 021314.
- [63] B. E. Treeby, J. Jaros, D. Rohrbach, and B. T. Cox, "Modelling elastic wave propagation using the k-Wave MATLAB Toolbox," in *Proc. IEEE Int. Ultrason. Symp.*, Sep. 2014, pp. 146–149.
- [64] W. R. Hendee and E. R. Ritenour, "Ultrasound waves," in *Medical Image Physics*, 4th ed. Hoboken, NJ, USA: Wiley, 2002.
- [65] J. W. Hunt, M. Arditi, and F. S. Foster, "Ultrasound transducers for pulse-echo medical imaging," *IEEE Rev. Biomed. Eng.*, vol. BME-30, no. 8, pp. 453–481, Aug. 1983.
- [66] M. Soumekh, *Synthetic Aperture Radar Signal Processing with MATLAB Algorithms*. 1st ed. New York: NY, USA: Wiley, 1999.
- [67] D. M. Sheen, D. L. McMakin, and T. E. Hall, "Three-dimensional millimeter-wave imaging for concealed weapon detection," *IEEE Trans. Microw. Theory Techn.*, vol. 49, no. 9, pp. 1581–1592, Sep. 2001.
- [68] M. Fallahpour and R. Zoughi, "Fast 3-D qualitative method for through-wall imaging and structural health monitoring," *IEEE Geosci. Remote Sens. Lett.*, vol. 12, no. 12, pp. 2463–2467, Dec. 2015.
- [69] H. Lee, *Acoustical Sensing and Imaging*. Boca Raton, FL, USA: CRC Press, 2016.
- [70] J. A. Jensen, S. I. Nikolov, K. L. Gammelmark, and M. H. Pedersen, "Synthetic aperture ultrasound imaging," *Ultrasonics*, vol. 44, pp. e5–e15, Dec. 2006.
- [71] L. J. Busse, "Three-dimensional imaging using a frequency-domain synthetic aperture focusing technique," *IEEE Trans. Ultrason., Ferroelectr., Freq. Control*, vol. 39, no. 2, pp. 174–179, Mar. 1992.
- [72] M. Soumekh, "Airborne synthetic aperture acoustic imaging," *IEEE Trans. Image Process.*, vol. 6, no. 11, pp. 1545–1554, Nov. 1997.
- [73] D. Garcia, L. L. Tarnec, S. Muth, E. Montagnon, J. Porée, and G. Cloutier, "Stolt's f-k migration for plane wave ultrasound imaging," *IEEE Trans. Ultrason., Ferroelectr., Freq. Control*, vol. 60, no. 9, pp. 1853–1867, Sep. 2013.
- [74] M. Fallahpour, J. T. Case, M. T. Ghasr, and R. Zoughi, "Piecewise and Wiener filter-based SAR techniques for monostatic microwave imaging of layered structures," *IEEE Trans. Antennas Propag.*, vol. 62, no. 1, pp. 282–294, Jan. 2014.
- [75] W. C. Chew and S.-Y. Chen, "Response of a point source embedded in a layered medium," *IEEE Antennas Wireless Propag. Lett.*, vol. 2, pp. 254–258, 2003.
- [76] Ö. Oralkan *et al.*, "Capacitive micromachined ultrasonic transducers: Next-generation arrays for acoustic imaging?" *IEEE Trans. Ultrason., Ferroelectr., Freq. Control*, vol. 49, no. 11, pp. 1596–1610, Nov. 2002.
- [77] M. Bassi, M. Caruso, A. Bevilacqua, and A. Neviani, "A 65-nm CMOS 1.75–15 GHz stepped frequency radar receiver for early diagnosis of breast cancer," *IEEE J. Solid-State Circuits*, vol. 48, no. 7, pp. 1741–1750, Jul. 2013.
- [78] B. Lu, Q. Song, Z. Zhou, and H. Wang, "A SFCW radar for through wall imaging and motion detection," in *Proc. 8th Eur. Radar Conf.*, Oct. 2011, pp. 325–328.

- [79] K. Iizuka, A. P. Freundorfer, K. H. Wu, H. Mori, H. Ogura, and V. K. Nguyen, "Step-frequency radar," *J. Appl. Phys.*, vol. 56, no. 9, pp. 2572–2583, Nov. 1984.
- [80] H. Nan, S. Liu, N. Dolatsha, and A. Arbabian, "A 16-element wideband microwave applicator for breast cancer detection using thermoacoustic imaging," in *Proc. (PIERS)*, Jul. 2015, pp. 243–247.
- [81] Y. Gong, P. Gao, L. Wei, C. Dai, L. Zhang, and Y. Li, "An enhanced adaptive filtering method for suppressing cardiopulmonary resuscitation artifact," *IEEE Trans. Biomed. Eng.*, vol. 64, no. 2, pp. 471–478, Feb. 2017.
- [82] B. Widrow *et al.*, "Adaptive noise cancelling: Principles and applications," *Proc. IEEE*, vol. 63, no. 12, pp. 1692–1716, Dec. 1975.
- [83] L.-P. Song, Q. H. Liu, F. Li, and Z. Q. Zhang, "Reconstruction of three-dimensional objects in layered media: Numerical experiments," *IEEE Trans. Antennas Propag.*, vol. 53, no. 4, pp. 1556–1561, Apr. 2005.
- [84] F. Li, Q. H. Liu, and L.-P. Song, "Three-dimensional reconstruction of objects buried in layered media using Born and distorted Born iterative methods," *IEEE Geosci. Remote Sens. Lett.*, vol. 1, no. 2, pp. 107–111, Apr. 2004.
- [85] Y. P. Chen, W. C. Chew, and L. Jiang, "A new Green's function formulation for modeling homogeneous objects in layered medium," *IEEE Trans. Antennas Propag.*, vol. 60, no. 10, pp. 4766–4776, Oct. 2012.
- [86] C. Yu *et al.*, "Active microwave imaging II: 3-D system prototype and image reconstruction from experimental data," *IEEE Trans. Microw. Theory Techn.*, vol. 56, no. 4, pp. 991–1000, Apr. 2008.
- [87] Q. H. Liu *et al.*, "Active microwave imaging. I. 2-D forward and inverse scattering methods," *IEEE Trans. Microw. Theory Techn.*, vol. 50, no. 1, pp. 123–133, Jan. 2002.
- [88] C. Pichot, L. Jofre, G. Peronnet, and J.-C. Bolomey, "Active microwave imaging of inhomogeneous bodies," *IEEE Trans. Antennas Propag.*, vol. 33, no. 4, pp. 416–425, Apr. 1985.



Ajay Singhvi (S'15) received the B.E. degree in electrical and electronics engineering from Birla Institute of Technology and Science Pilani, India in 2015. He is currently working toward the M.S./Ph.D. degree in electrical engineering from Stanford University.

From 2014 to 2015, he performed research at the University of Southern California and Birla Institute of Technology and Science Pilani, where he worked on the design of low power asynchronous circuits.

His current research is geared toward the design of integrated circuit systems for non-contact thermoacoustic and ultrasound imaging applications.



Kevin C. Boyle (S'15) graduated from Cornell University with the B.S. degree in electrical and computer engineering in 2014, studying ultra low power sensors and angle sensitive pixels. Afterwards, he started his Ph.D. degree in electrical engineering at Stanford University on thermoacoustic imaging at a standoff. He currently works on optical interferometry for detection and imaging of the mechanical deformation of a neuron that accompanies its action potential.



Mojtaba Fallahpour (M'14) received the Ph.D. degree in electrical engineering from Missouri University of Science and Technology in 2013.

In Summer 2012, he interned at Signal Integrity Group at Micron Technology Inc., and later in Fall 2012, he interned at Signal Integrity Group at Cisco Systems Inc. After graduation, he was with the University of Illinois at Urbana-Champaign (2013–2015) and Stanford University (2016–2017), as a Postdoctoral Research Associate. He is currently working at ANSYS Inc.



Butrus (Pierre) T. Khuri-Yakub (F'95) received the B.S. degree from the American University of Beirut, the M.S. degree from Dartmouth College, and the Ph.D. degree from Stanford University, all in electrical engineering.

He is currently a Professor of Electrical Engineering at Stanford University. His current research interests include medical ultrasound imaging and therapy, ultrasound neuro-stimulation, chemical/biological sensors, gas flow and energy flow sensing, micro-machined ultrasonic transducers, and ultrasonic fluid

ejectors. He has authored over 600 publications and has been principal inventor or co-inventor of 99 U.S. and international issued patents.

Prof. Khuri-Yakub was awarded the Medal of the City of Bordeaux in 1983 for his contributions to Nondestructive Evaluation, the Distinguished Advisor Award of the School of Engineering at Stanford University in 1987 the Distinguished Lecturer Award of the IEEE UFFC Society in 1999, a Stanford University Outstanding Inventor Award in 2004, Distinguished Alumnus Award of the School of Engineering of the American University of Beirut in 2005, Stanford Biodesign Certificate of Appreciation for commitment to educate mentor and inspire Biodesign Fellows in 2011, recipient of IEEE Rayleigh award 2011, and elected Fellow of the AIMBE in 2015.



Amin Arbabian (SM'17) received the Ph.D. degree in EECS from UC Berkeley in 2011.

In 2012 he joined Stanford University, as an Assistant Professor of Electrical Engineering, where he is also a School of Engineering Frederick E. Terman Fellow. In 2007 and 2008, he was part of the initial engineering team at Tagarray, Inc. He spent summer 2010 at Qualcomm's Corporate R&D division designing circuits for next generation ultra-low power wireless transceivers. Amin's research interests are in high-frequency circuits, systems, and

antennas, medical imaging, and ultra-low power sensors. He currently serves on the TPC for the European Solid-State Circuits Conference and the Radio-Frequency Integrated Circuits (RFIC) Symposium.

Prof. Arbabian is the recipient/co-recipient of the 2015 NSF CAREER award, 2014 DARPA Young Faculty Award (YFA), 2013 IEEE International Conference on Ultra-Wideband (ICUWB) best paper award, 2013 Hellman Faculty Scholarship, 2010 IEEE Jack Kilby Award for Outstanding Student Paper at the International Solid-State Circuits Conference, two time second place Best Student Paper Awards at 2008 and 2011 RFIC symposiums, the 2009 CITRIS (Center for Information Technology Research in the Interest of Society at UC Berkeley) Big Ideas Challenge Award and the UC Berkeley Bears Breaking Boundaries award, and the 2010–11 as well as 2014–15 Qualcomm Innovation fellowships.